

Mahalanobis distance among the phase portraits as damage feature

Riya C George, Sudib K Mishra and Mohit Dwivedi

Abstract

A number of damage-sensitive features have been proposed based on the damage-induced changes in the phase portrait, reconstructed from the measured dynamic responses of structure. Of a number of alternatives, the change in phase space topology is the most widely acclaimed for assessment of structural health. In this study, a damage feature is proposed by contrasting the damaged phase portrait with the pristine one. The contrast is expressed using the Mahalanobis distance measure, which is remarkably simpler than the change in phase space topology in algorithmic aspect. The feature is referred as Mahalanobis distance among the phase portraits. The performance of the feature is demonstrated by its sensitivity and localization of damage. The noise immunity study reveals reasonable tolerance to the measurement noise. The feature is numerically illustrated on a shear building subjected to Lorentz chaotic excitations and natural wind excitations. The feature is experimentally verified in a railway bridge model subjected to moving wheel load of a model train. The results show the effectiveness of the feature for localizing both the support damage (as in bearing) and damage in the span. Simple analytical argument is also provided to link the phase portrait distortion with the extent and localization of damage(s).

Keywords

Phase portrait, Mahalanobis distance, structural interrogation, statistical robustness, noise immunity

Introduction

The condition of structures needs to be monitored for its changes in stiffness, strength, or geometric properties to ensure safe performance during its lifetime. The procedure is referred as structural health monitoring (SHM). The SHM is also important to avoid downtime of the structure. Conventionally, a number of non-destructive techniques are employed along with visual inspection to assess the general condition of structures without quantitative estimate. The conventional non-destructive techniques require access to the structure, and all types of damages cannot be detected by such techniques. Modern SHM methodologies assess the structural health based on continuously monitored responses at strategic locations of structures in automated manner. The SHM methodologies are also employed for rapid assessment of structures after experiencing extreme events, such as earthquake and cyclone, to decide on their safe occupancy and reuse.

A number of sensors are installed on the structure for the purpose of SHM. The sensed responses are subsequently processed to extract the damage information. The robustness of SHM methodology is assessed with

respect to localization and detection of severity. Modern SHM involves several components, such as sensing of responses, acquisition of sensed responses, extraction of damage information, and prognosis of the structure. However, the challenge to the structural engineers is the analysis of these responses for extracting useful information regarding damage(s).^{1,2} A number of techniques extract damage-sensitive features from the measured responses and correlate them with the presence and location of damage(s). The change in natural frequencies,³ change in mode shape curvature,⁴ auto regressive and moving average coefficients in predictive model,⁵ and wavelet-based techniques⁶ are to name a few. An exhaustive review of the available techniques is provided in Doebling et al.¹ and Sohn et al.²

Department of Civil Engineering, Indian Institute of Technology Kanpur, Kanpur, India

Corresponding author:

Sudib K Mishra, Department of Civil Engineering, Indian Institute of Technology Kanpur, Kanpur 208016, Uttar Pradesh, India.

Email: smishra@iitk.ac.in

Recently, several features based on the phase space representation of structural dynamics are reported in the literature. These are commonly referred as phase space features, and the respective procedure is referred as phase space interrogation. The dynamical states of a structure trace out certain geometry in its phase space during motion and such representation is known as phase portrait. Nichols⁷ has demonstrated that damage in a structure can be attributed to changes in the properties of the phase portraits. The improved sensitivity of the phase space-based features is established over the conventional modal features by Todd et al.⁸ Another important aspect is that the phase space analysis does not rely on linearity of structural behavior unlike modal features. A number of damage features are derived based on disparities among the phase portraits from the damaged and pristine structure. The local attractor variance ratio proposed by Todd et al.⁸ and Nichols,⁷ the phase space warping suggested by Chelidze and Liu,⁹ and the change in phase space topology (CPST) by Nie et al.^{10,11} are the phase portrait-based damage features. However, previous studies require the structures to be excited by a low-dimensional chaotic signal to ensure low dimensionality of the phase portrait. Usage of ambient or natural excitations is relatively restricted, and the only study till date is by Nichols.⁷ However, the phase space interrogation methodology is also extended for structures subjected to stochastic excitations. This is presented by Overbey et al.¹² and Liu et al.¹³ Improved damage sensitivity is also achieved by employing hyper-chaotic excitation by Torkamani et al.¹⁴ Of all damage features, the CPST^{10,11} is the most simple and consistent and is most widely employed for the purpose of damage detection. In this study, a new damage-sensitive feature is proposed based on probabilistic distance measure among the phase portraits, which is much simpler to compute than the conventional CPST. The probabilistic distance measure employed herein is the Mahalanobis distance (MD).¹⁵ The choice of MD is motivated from its properties of scale invariance, consideration of the correlation among the datasets, and the distance measurements along the principal component axis in the point cloud, as in the phase portrait. It may be mentioned that the application of the MD in marking an outlier in the context of SHM has been attempted by Banerjee et al.¹⁶

The damaged and pristine phase portraits are reconstructed from the measured responses of the structure using Takens'¹⁷ embedding theorem. The reconstructed phase portraits from the measured responses are referred as embedded phase portrait. The MD among the point clouds pertaining to the damaged and pristine phase portraits is evaluated. It is observed that the MD among the portraits shows considerable sensitivity to

the induced damage scenarios as it varies almost proportionally with the severity of damage. The sensitivity is much higher than the conventional CPST. The localization obtained by this feature is observed to be much sharper. Furthermore, computation of the MD is significantly less intensive than the CPST.

A multistoried shear building is employed for the numerical elucidation. The building is analyzed for its dynamic responses under chaotic (Lorentz) excitations as well as low-dimensional (narrow-band) natural wind excitations. A number of damage scenarios of varying severity and locations are inflicted by reducing the column stiffness along various stories. The structural responses from the pristine and damaged buildings are subsequently processed in search of the incipient damage(s), their localization, and relative estimate of severity. The phase portraits are reconstructed from these responses. The robustness of the feature is also assessed using experimentally observed responses from a railway bridge model subjected to train loading and inflicted with a number of alternative damage scenarios. This involves damage at the supports (bearings) as well as in the span (bridge deck). The trends portrayed by the experimental results corroborate well with the numerical analysis. The details are presented subsequently. Finally, a simple analysis is also presented in Appendix 1 that analytically establishes the link of the distortion of phase portraits with the damage.

Phase portrait from measured responses and extraction of the feature

The phase space interrogation involves several steps, presented in some detail in the following sections. It is to be mentioned that the simulated responses from the dynamic analysis of the structure subjected to chaotic and wind excitations are made use of in this study. For numerical elucidation, the simulated responses of a shear building subjected to these excitations are employed. It may be noted that these responses are low dimensional and amenable to phase space embedding.

The excitation time histories of the chaotic and the wind excitations are simulated numerically. The responses of the shear building are obtained under both types of excitations, subsequently analyzed through singular system analysis to ascertain on the dimensionality of embedding. This follows the Takens' embedding theorem.^{17,18} The lag coordinate is obtained from the average mutual information function of the response time histories. With the embedding dimension and the lag, the phase portraits are reconstructed. The reconstructed phase portraits from the responses of structures are analyzed and contrasted using the MD.

The chaotic Lorentz and wind excitations

The simulated dynamic responses of the structure along different stories are obtained by subjecting the structure to chaotic or wind excitations. A number of alternative chaotic systems (e.g. Lorenz system, Duffing system) are employed for this purpose. The Lorenz system is employed presently. This system is governed by a set of nonlinear ordinary differential equations as¹⁹

$$\begin{aligned}\dot{x} &= \sigma(y - x) \\ \dot{y} &= x(\rho - z) - y \\ \dot{z} &= xy - \beta z\end{aligned}\quad (1)$$

where the dot (.) over a symbol implies its time derivative, and x , y , and z are the state variables. The symbols σ , ρ , and β are the parameters of the system. The system is numerically integrated to obtain the time histories of these states. Any one among these (with proper scaling for its magnitude and dominant frequency) may be employed as the exciting signal. Specific values of the system parameters are chosen to ensure chaotic behavior. The excitation is assumed to be applied at the top storey of the structure. For implementation, such excitations may be achieved by placing mass shakers or actuator at the specific story level.

The natural wind excitations retain more appeal as this does not require external excitations. The wind force acting ($F(z, t)$) at a story level at height (z) can be expressed as

$$F(z, t) = \rho A c_p \bar{V}(z) v(z, t) \quad (2)$$

in which $\bar{V}(z)$ is the mean wind speed and $v(z, t)$ is the fluctuating part. The symbol ρ is the density of air; A is the tributary area for the structural node, over which the wind pressure is acting; and c_p is the coefficient of wind pressure. The estimated wind forces are applied along the stories. The wind speed $V(z, t)$ at a height z of the structure may be regarded as the sum of a mean wind speed $\bar{V}(z)$ and a fluctuating component $v(z, t)$ as

$$V(z, t) = \bar{V}(z) + v(z, t) \quad (3)$$

The fluctuating wind velocity field $v(x, y, z, t)$ in a structure should ideally be treated as a multidimensional, multivariate stochastic process.²⁰ However, for a two-dimensional frame structure, the wind loading is simplified as an independent, one-dimensional, multivariate (for different stories) stochastic processes. Out of several alternative procedures for digital simulation, the spectral representation technique is adopted presently.²¹

The one-dimensional, multivariate, zero mean wind speed process $\{v(z, t)\}$ can be sufficiently described by its cross-spectral density matrix $[S(\omega)]$ at each exciting

frequency (ω). The off-diagonal terms $S_{ij}(\omega)$ are the cross-spectral density among the i th and j th floors, and the diagonal terms are the auto-spectral densities. The fluctuating wind velocity components $v(z_i, t)$ at the i th floor with height z_i are simulated as²¹

$$v(z_i, t) = \sqrt{2\Delta\omega} \sum_{m=1}^i \sum_{l=1}^{n_\omega} |H_{im}(\omega_{ml})| \cos(\omega_{ml}t - \theta_{im}\omega_{ml} + \Phi_{ml}); i = 1, 2, \dots, n \quad (4)$$

In this expression, n is the number of stories; n_ω is the number of frequency components defining the frequency resolution ($\Delta\omega$), $\Delta\omega = \omega_u/n_\omega$; ω_u is the cut-off frequency beyond which the power spectral density ordinates can be neglected. The symbol Φ_{ml} are the sequences of independent random phase angles uniformly distributed over the interval $[0, 2\pi]$. The symbol $H_{im}(\omega_{ml})$ is used to define the elements of the matrix $[H(\omega)]$, obtained by the Cholesky decomposition of the matrix $[S(\omega)]$. The discrete frequency components (ω_{ml}) are obtained as $\omega_{ml} = (l-1)\Delta\omega + (m/n)\Delta\omega$; $l = 1, 2, \dots, n_\omega$. In this work, the online portal (*NatHaz*) at the University of Notre Dame for wind load simulation, provided by Kwon and Kareem,²² is used for simulating the wind velocity field. The simulation uses the Kaimal velocity spectra. More details of this can be found elsewhere.²² While the diagonal terms in the matrix $[S(\omega)]$ are given by the Kaimal spectra, the cross-spectral densities ($S_{ij}(\omega)$) are obtained from the coherency function ($\gamma_{ij}(\omega)$), defined as

$$\gamma_{ij}(\omega) = \frac{S_{ij}(\omega)}{\sqrt{S_{ii}(\omega)S_{jj}(\omega)}} \quad (5)$$

The coherency function defines the cross correlation among the two wind speeds at the respective storey height. The Davenport's coherence function²³ is presently adopted for this.

Dynamic analysis of the structure for simulation of responses

For monitoring, the dynamic responses of the building under excitations are considered. The structure is assumed to be linear with viscous damping. The equation of motion is written as

$$[M]\{\ddot{u}\} + [C]\{\dot{u}\} + [K]\{u\} = \{P\} \quad (6)$$

in which $[M]$, $[C]$, and $[K]$ are the mass, damping, and stiffness matrix, respectively; $\{\ddot{u}\}$, $\{\dot{u}\}$, and $\{u\}$ are the relative acceleration, velocity, and displacement vector pertaining to lateral degrees of freedoms, respectively. The forcing vector $\{P\}$ is the lateral forcing from the chaotic or wind loading. The equations of motion in

equation (6) are integrated numerically in time by the step-by-step integration method. The time step (Δt) is adopted by ensuring stability of the algorithm. The Hilbert–Hughes–Taylor (HHT) algorithm is employed presently for this purpose.

Unlike simulated responses ($s(t)$), the measured response signals ($s_m(t)$) are likely to be contaminated by noise ($n(t)$) from various sources. The noisy sensor measurement of responses can be expressed as

$$\{s_m(t)\} = \{s(t)\} + \{n(t)\} \quad (7)$$

in which $\{n(t)\}$ is the sensor noise vector, the elements of which are either Gaussian or white noise with root mean square (r.m.s.) value as fraction of the r.m.s. of the original response signal. The magnitude of the noise is described by the signal-to-noise ratio (SNR) and is expressed as

$$\text{SNR} = 10 \log_{10} \left(\frac{\sigma_s}{\sigma_n} \right)^2 = 20 \log_{10} \left(\frac{\sigma_s}{\sigma_n} \right) \quad (8)$$

in which $\sigma_{s(t)}$ and $\sigma_{n(t)}$ are the r.m.s. values of the response signal ($s(t)$) and the noise ($n(t)$), respectively. The unit decibel is used for the SNR. The noise-contaminated responses are employed as input in the interrogation.

Reconstruction of the phase portrait from the responses

The governing equation of motion of the structure is a second-order system, which can also be cast into two first-order systems. The first-order equations describe the evolution of the displacements and velocities and the complete dynamics thereof. While plotted in a displacement–velocity space (referred as phase space), the evolution will trace out certain geometry, referred as phase portrait. However, as there is no explicit consideration of time, the information on the rate of evolution is lost in such representation. Nevertheless, many important information and insight regarding the system behavior can still be derived from such representation.

The equation of motion of the structure (equation (6)) can be written in the state-space form

$$\frac{dx(t)}{dt} = F(x(t)); x(t) \in R^n \quad (9)$$

The system can be written in discrete time as

$$F: R^n \rightarrow R^n; x(t+1) = f(x(t)); t \in 0, 1, \dots \quad (10)$$

Let $x(t+m) = f^m(x(t))$ and a subset of $y(t)$ is defined as

$$h: R^n \rightarrow R; y(t) = h(x(t)) \quad (11)$$

The subsystem in m dimension can be represented as $y^m(t) = (y(t+m-1), y(t+m-2), \dots, y(t))$, forming a subsystem out of the compact manifold U . For $m \geq 2n+1$

$$\begin{aligned} J^m(x(t)) &= y^m(t) \\ &= (h(f^{m-1}(x(t))), h(f^{m-2}(x(t))), \dots, h(x(t))) \end{aligned} \quad (12)$$

This defines an embedding from U to $J^m(U)$. There will exist a functional g so that

$$y^m(t+1) = g(y^m(t)) \quad (13)$$

It may also be observed that

$$y^m(t+1) = J^m(x(t+1)) = J^m(f(x(t))) \quad (14)$$

and therefore

$$J^m(f(x(t))) = g(J^m(x(t))) \quad (15)$$

Functional f and g are said to be topologically isomorphic and preserving the dynamical characteristics of both. The operator J^m is said to be homeomorphic. Several dynamical invariants of the original phase portrait can also be computed from the reconstructed portrait. It is mentioned that the construction of phase portrait requires measuring a large number of responses that might not be practically feasible. However, it is observed that the qualitative behavior of the phase portrait is captured based on the limited number of measurements. This is the celebrated Takens' theorem^{17,18} for embedding phase portrait.

Following this theorem, a measured time series $\{x\}$ can be embedded into a (pseudo)-phase space of dimension (m_d) with appropriate lag (τ). The parameters, embedding dimension (m_d) and the lag coordinate (τ), are determined from the singular system analysis and the average mutual information function of the measured response time histories, respectively. A circulant matrix from the measured responses is formed for the singular analysis, in which the number of columns is decided by the responses, sampled over a time window of length ($q = f_s \tau_f$), obtained from the product of the sampling frequency (f_s) and a parameter (τ_f). The latter depends on the maximum frequency content ($\tau_f \leq 1/f^*$) in the signal. The circulant matrix $[A]$ can be decomposed by the singular value decomposition to obtain the singular values ($\sigma_i, i = 1, \dots, q$), normalized by their sum. Smaller values imply noise, whereas the dominant ones are attributed to the active dynamical degrees of freedom, which are counted as the embedding dimension (m_d) for the phase portrait reconstruction.

The lag coordinate (τ) for reconstruction is based on the average mutual information function of the signal. This is defined as a function of the time lag (T) as^{24,25}

$$I(\tau) = \sum_{nt} p(x(i), x(i+\tau)) \log_2 \left(\frac{p(x(i), x(i+\tau))}{p(x(i))p(x(i+\tau))} \right) \quad (16)$$

in which $p(x(i))$ and $p(x(i+\tau))$ are the probability densities of $x(i)$ and $x(i+\tau)$, and $p(x(i), x(i+\tau))$ is the joint probability density. This time lag corresponds to the first minima of the information function and is chosen as the lag for embedding. This is in account of the fact that the minimum information function indicates to the point corresponding to the reduced level of statistical dependency. Optimal delay ensures that the phase portrait is completely unfolded in the phase space. Embedding a portrait using too less lag results in trajectories being falsely projected on another part.

It is important to note that the embedding theorem assumes that the dynamics of the system is deterministic. For stochastic excitation, the embedding theorem cannot be used in principle. It is also demonstrated that the number of points (N_p) required to accurately describe a phase portrait scales in power of its embedding (m_d) dimension.²⁶ The expression implies that a system with modest dimension requires prohibitively large data to accurately represent the underlying dynamics. The chaotic excitations/responses being low dimensional are free from the curse of dimensionality. For structures under stochastic excitation, the dimension cannot be controlled. However, Nichols⁷ showed that the embedding theorem is still employed for stochastically driven system, especially if the process is narrow band and can be treated as low dimensional. Trickey et al.²⁵ showed that responses of a structure under narrow-band excitations result in practically low-dimensional responses that can be embedded using few dimensions. Stark et al.²⁷ extended Takens' embedding theorem for stochastically driven system. Orstavik and Stark²⁸ demonstrated that a 70-dimensional system can be mimicked through a 4-dimensional system through optimal modeling. Although the wind excitations and the responses are stochastic, they are relatively low dimensional and can be embedded in low-dimensional phase space for subsequent analysis.

Extraction of damage features: MD among the phase portraits

The dynamics of the structure is bound to change due to any damage(s) which will be reflected in the disparities among the phase portraits from the pristine and damaged structures. This disparity is quantified as the damage-sensitive feature. Of several alternatives, the dissimilarity among the topology of the phase portrait using CPST is the most conveniently employed in the earlier study. Details of the algorithmic aspects for computation of the CPST can be obtained from the literature.⁸ This study proposes the use of MD metric to

measure the distance among the point clouds pertaining to the reconstructed phase portraits.

Conventionally, the MD was formulated to measure the distance of an individual point from a distributed point cloud to check how far that point is from the representative population. A number of realizations $\{\{x\}^1 \{x\}^2 \dots \{x\}^n\}$ of a random vector $\{X\}$ may be obtained from observations of a random experiment. The statistics of this random vector is estimated as the mean $\{\mu_X\}$ and the covariance matrix $[C_{XX}]$. Thereafter, a particular realization of the same experiment may be obtained as $\{x\}^i$. The distance of this observation from the dataset (whose statistics have already been obtained) can be expressed as¹⁵

$$D_M(\{x\}^i) = \sqrt{(\{x\}^i - \{\mu_X\})^T [C_{XX}]^{-1} (\{x\}^i - \{\mu_X\})} \quad (17)$$

The above definition of the MD can also be generalized to find the dissimilarity measure between two realizations $(\{z\}^i, \{z\}^j)$ of a random vector $\{Z\}$ as

$$d_M(\{z\}^i, \{z\}^j) = \sqrt{(\{z\}^i - \{z\}^j)^T [C_{ZZ}]^{-1} (\{z\}^i - \{z\}^j)} \quad (18)$$

Since these vectors have identical distribution, they will have same covariance matrix $[C_{ZZ}]$. For diagonal covariance matrix, the MD reduces to the Euclidean distance. It is clear that given a test point in Euclidean space, in which there already lies a population of points, the MD among the test point with that of the population provides an idea as how much the test point is closer to the population. Due to this property, the MD appears to be a suitable measure to be adopted in outlier analysis. If the distance between the test point and the center of mass (of a population) is less than certain threshold value, the point can be taken to belong to the set.

Conventionally, the normalized distance between a test point (x) and the center of mass of the set μ may be defined as $((x - \mu)/\sigma)$, which may be substituted into the normal distribution to estimate the probability of whether the test point belongs to the set or not. Such estimate assumes that the distribution of the points is spherical around their centroid. This assumption may not be valid for non-spherical distribution, such as ellipsoidal. Expectedly, the probability of belonging to one set depends not only on the distance from the centroid but also on its directional orientation. For example, in case of ellipsoidal distribution, the distance will be less along the minor axis but more when aligned along the major axis. While devising the MD, this aspect is taken care by weighting the distances by their corresponding covariance terms. These terms represent the directional

orientations by implicitly incorporating the widths of the ellipsoidal population along the directions of the test point.

From the embedding of the phase portraits, the observations of the coordinate vectors of each point from the pristine and damaged structures are written in matrix form as $[x_u]$ and $[x_d]$, respectively. These matrices are of dimension (m, n_d) , where n_d is the number of embedding dimension (coordinates) equal to the number of columns in the matrix. The number of rows (m) is the number of points sampled on the embedded phase portrait (EPP). Thus, each column contains the coordinates, and the observations/realizations are put along the rows of the matrix. The phase portrait from the pristine and damaged structures is to be contrasted using suitable metric. It may be recalled that the distribution of the points on the phase portraits is not necessarily spherical around their centroid, which is coincident to the origin. Therefore, estimating the distance is significantly affected by the asymmetry in the distribution of the point cloud in the phase portrait. Furthermore, the scale invariance of the distance metric is another desirable property, while contrasting the phase portraits. Taken together, the MD will ideally suit the present purpose. In applying the MD for contrasting the phase portraits, slight modifications are needed on the basic framework as, explained subsequently.

The coordinates of the pristine and damaged phase portraits are denoted by two random vectors as $\{X\}_p$ and $\{X\}_d$. Each point on these phase portraits is re-treated as a single realization of these coordinate vectors, denoted as $\{x\}_p$ and $\{x\}_d$ for the pristine and damaged portraits, respectively. The centroid of these portraits is obtained from the mean of these random vectors, denoted as $\{\mu\}_p$ and $\{\mu\}_d$, respectively. The coordinates of the center of masses $\{\mu\}_p$ and $\{\mu\}_d$ can also be treated as realization of two random vectors, denoting the coordinates of the center of mass. From the realizations of the random coordinate vectors $\{X\}_p$ and $\{X\}_d$, their covariance matrices can also be estimated as $[C_{X_p X_p}]$ and $[C_{X_d X_d}]$, respectively. Given the type of distortion in phase portrait induced by damage, these two estimates are not supposed to vary significantly. However, for estimation of the MD, a single weighted covariance matrix is obtained by assigning relative weights to each of these covariance matrices. This is expressed as

$$[C_{WW}] = w_1 [C_{X_p X_p}] + w_2 [C_{X_d X_d}] \quad (19)$$

The weight factors are decided based on the relative number of points sampled in each phase portrait over the total number of points sampled in both. For the present purpose, equal weights are assigned to each and hence $w_1 = w_2 = 0.5$. The weighted covariance is often

referred as pooled covariance in finance literature.²⁹ The MD among the phase portraits is then defined as

$$D_{PM} = \sqrt{\left(\{\mu_p\} - \{\mu_d\}\right)^T [C_{WW}] \left(\{\mu_p\} - \{\mu_d\}\right)} \quad (20)$$

This slightly modified version of the MD is adopted to be a damage feature in this study. The legitimacy of the feature is first established with respect to its monotonicity with increasing degree of damage(s). The localization capability (both single and multiple damages) is also assessed. The robustness of the MD-based feature is also scrutinized under alternative sources of excitations as well as parametric variations. Details of these are presented in the subsequent sections.

Numerical illustration

The phase space interrogation methodology based on MD is numerically illustrated using a multistoried, shear building frame with varying degrees of induced damage. The damage(s) are induced by reducing its column stiffness to desired degree. The 10-storied shear building with appropriate mass and stiffness distribution is chosen to have its fundamental time period around 0.78 s. The relatively higher period is intended in view of its sensitivity to long period wind excitations as well as excitations from the Lorentz chaotic excitations.

The Lorentz chaotic excitations are generated using the procedure described in section "The chaotic Lorentz and wind excitations." The parameters adopted for the Lorentz system are $\sigma = 10$; $r = 28$; $b = 8/3$; $\delta = 1$ to allow chaotic behavior. The chaotic behavior is ascertained with positive Lyapunov exponent of the time history responses. The wind loading along the stories are simulated following the procedure illustrated previously. The numerical values of the parameters adopted for simulation of wind excitations are provided as follows: the cut-off frequency (ω_u) is 5 Hz, the time step for simulation (Δt) is 0.05 s, and the total duration of the time history is 200 s. The exposure category (as per ASCE 7-98) is adopted to be C. The value of the gust wind speed is also varied from 5 and 10 m/s for parametric study. The power law distribution of the mean wind velocity profile is adopted along the height of the building. A schematic of the shear building, associated excitations, and the installation of sensors for response measurement is depicted in Figure 1.

The time history of forcing from the Lorentz system is shown in Figure 2(a), along with the structural responses at a typical story in Figure 2(b). It may be noted that the Lorentz-type excitations can be simulated in a real building using mass shaker of appropriate capacity, mounted on the top of the building to be

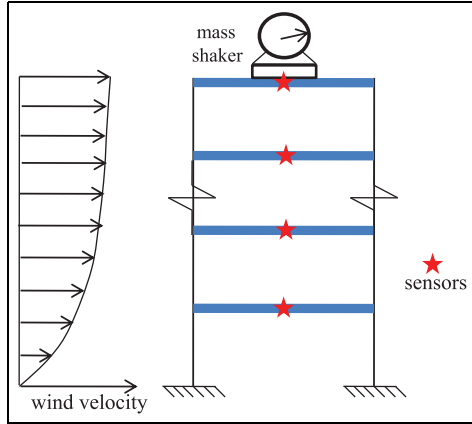


Figure 1. Schematic diagram of a shear building with wind excitations and excitations from mass shaker/actuators. The sensor deployment for response measurement at locations is shown.

interrogated. At specific story, such excitations may be exerted by actuator of specific capacity. The low dimensionality of the excitation and the responses may be observed from these plots. Typical time histories of the fluctuating component of the simulated wind speed at a story (fifth) are also shown in Figure 2(c) and the respective response of the building at that location is shown in Figure 2(d). The dynamic analysis of the building subjected to the simulated Lorentz/wind excitations is performed using the Newmark beta time integration by adopting a time step of 0.05 s, ensuring stability and reasonable accuracy.

The total length of the data for both types of excitations is 4000. For the chaotic response, the excitation is applied at only one point (at the top of the building), whereas wind excitations are applied along all the stories. For chaotic excitations, only one type of wave form is employed, whereas for wind two alternative mean wind speeds are employed. It may be reminded that tall wind-sensitive building may experience severe $P - \delta$ effect due to inclusion of geometric nonlinearity, which is not accounted for in this analysis.

Although the floor acceleration time histories at each story are the natural choices as input for the structural interrogation, presently, the time histories of the individual story drifts are employed. The drift time histories are calculated from the displacement time histories along various stories of the building. The choice of the drift is partially motivated by the fact that the dimensionality of the storey drifts is much lower than the floor acceleration, hence amenable to low-dimensional embedding. Furthermore, if the story drifts are calculated from the measured acceleration responses, the effect of measurement noise will be suppressed due to the process of integration. However, with the

development in measurement techniques, direct measurement of the displacements along the stories is also feasible using laser-based vibrometer. The performance of the conventional contact devices (e.g. accelerometer) with the laser-based non-contact devices is discussed by Nassif et al.³⁰ for the health monitoring purpose. A recent study involving in situ displacement response for condition updating of railway bridge by Feng and Feng³¹ is notable. A recent study by George and Mishra³² and Paul et al.³³ in the context of phase space interrogation also employed the displacements both for simulation and experimental verification.

The response time histories along all the stories are analyzed in search of damage features derived from the phase portraits. For this, the singular system analysis is performed on the response signals to obtain the estimate of the required dimension for the embedding for the phase portrait. This also helps in testing the viability of low dimensionality. The average mutual information function for the story drift time histories is obtained to estimate the necessary lag for embedding. The normalized singular spectrum and the mutual information function for the typical story drifts are shown in Figure 3(a) and (b) and Figure 3(c) and (d), for the Lorentz excitation and wind excitation-induced responses, respectively. It may be observed that the phase portrait reconstruction is possible only with a fewer number of embedding dimensions, which can be taken between four and six depending on the threshold chosen for the normalized singular value. Presently, the embedding dimension is adopted to be five for both. The plot of average mutual information function (Figure 3(b) and (d)) shows that the delay coordinates can be taken as 20 and 10 for the Lorentz and wind-induced responses, respectively. These correspond to the first minima of the respective average mutual information functions.

With the estimated embedding dimensions and the lags, the reconstructed phase portraits are shown in Figure 4(a) and (b) for the Lorentz and wind excitation-induced responses, respectively. For demonstration, a three-dimensional embedding is chosen, although the actual dimension of embedding is much larger. The first set of damage scenarios considered in this study is obtained by reducing the lateral stiffness of the columns at fifth story. The amount of reduction quantifies the extent of damage, which is varied from 5% to 25%. The time histories of the respective responses along the stories are employed for reconstruction of the damaged and undamaged phase portraits. Subsequently, the MD among the phase portraits values is estimated for the damaged structures with 5%, 10%, 15%, 20%, and 25% damage. The variations in the MD among the phase portraits corresponding to these increasing intensities of damage(s)

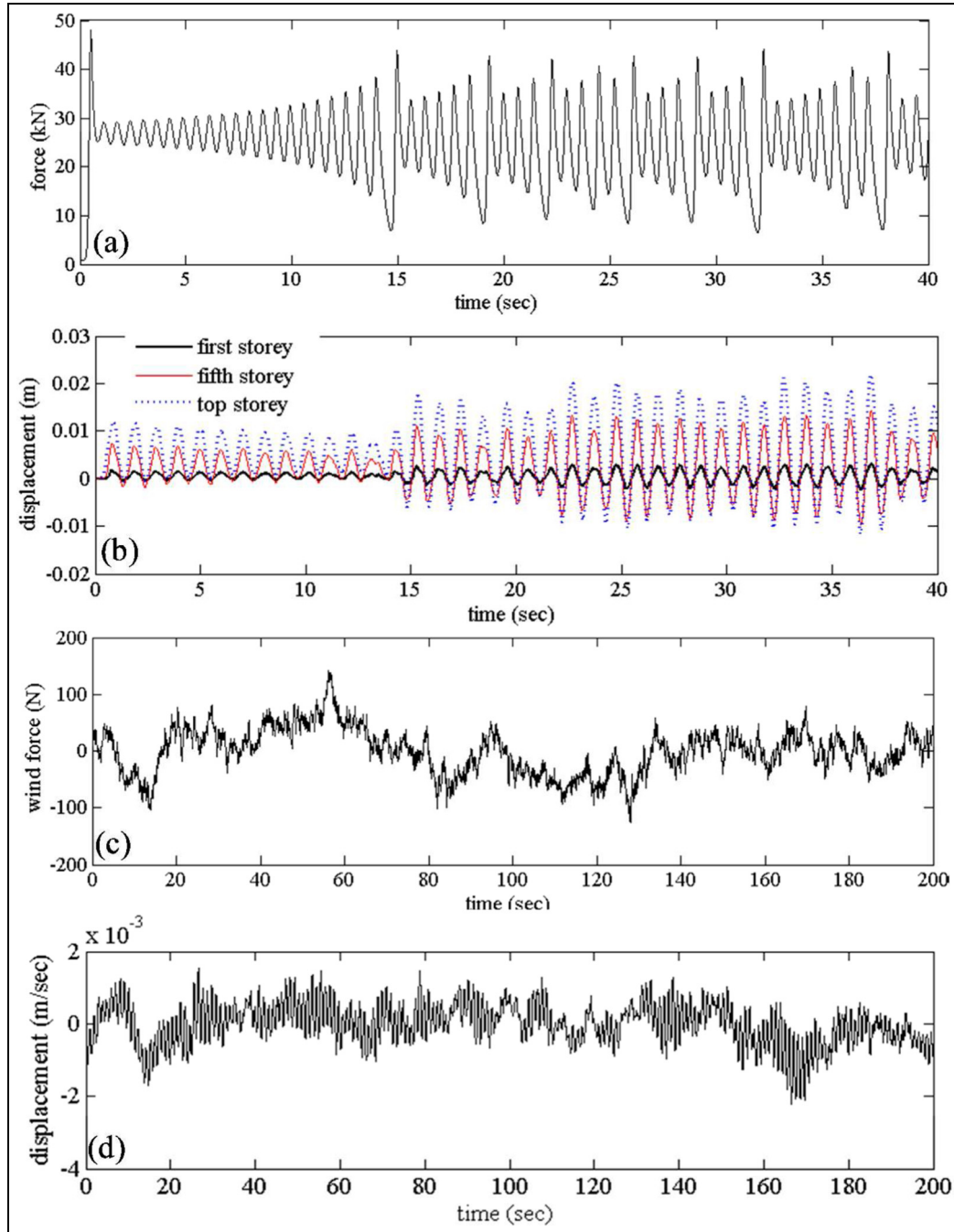


Figure 2. Time histories of (a) Lorentz chaotic excitation and (b) respective response time histories. (c) Fluctuating component of the wind forcing and (d) typical response time history of the structure at a story.

are shown in Figure 5(a) and (b) for Lorentz and wind excitations, respectively.

It is observed from Figure 5(a) and (b) that with increasing level of damage, the MD among the phase portraits increases monotonically. This is an essential trend that must be portrayed by any legitimate damage feature, and the MD among the pristine and damaged phase portraits qualifies for this. It may also be noted

that with increasing damage level, the MD damage metric increases monotonically for both types of excitations. Furthermore, with increasing intensities of excitations (i.e. higher speed of wind), the sensitivity of the feature enhances. The slope of the damage versus MD among phase portraits' plot becomes more steeper with increasing gust speed of wind, as shown in Figure 5(b).

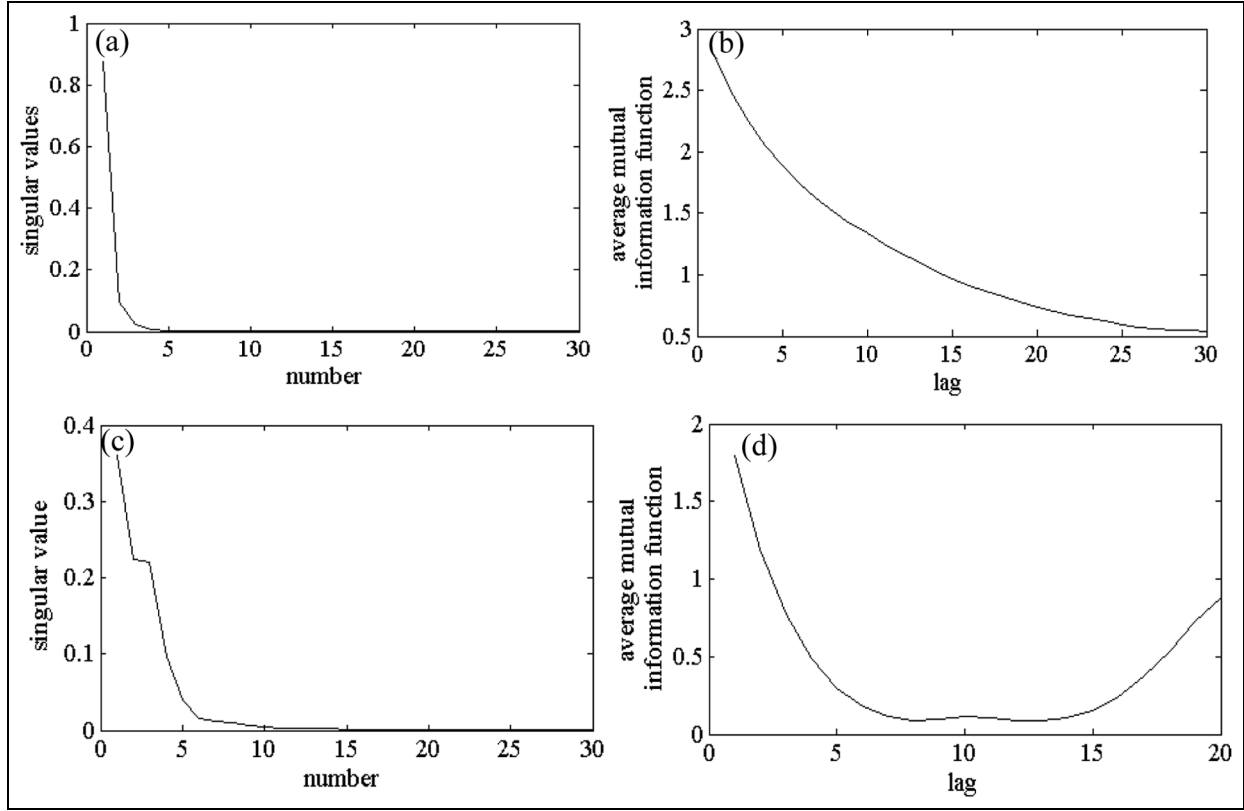


Figure 3. (a) Singular value spectrum and (b) the average mutual information function for the Lorentz excitation-induced responses. (c) Singular spectrum and (d) the average mutual information function for the wind-induced responses.

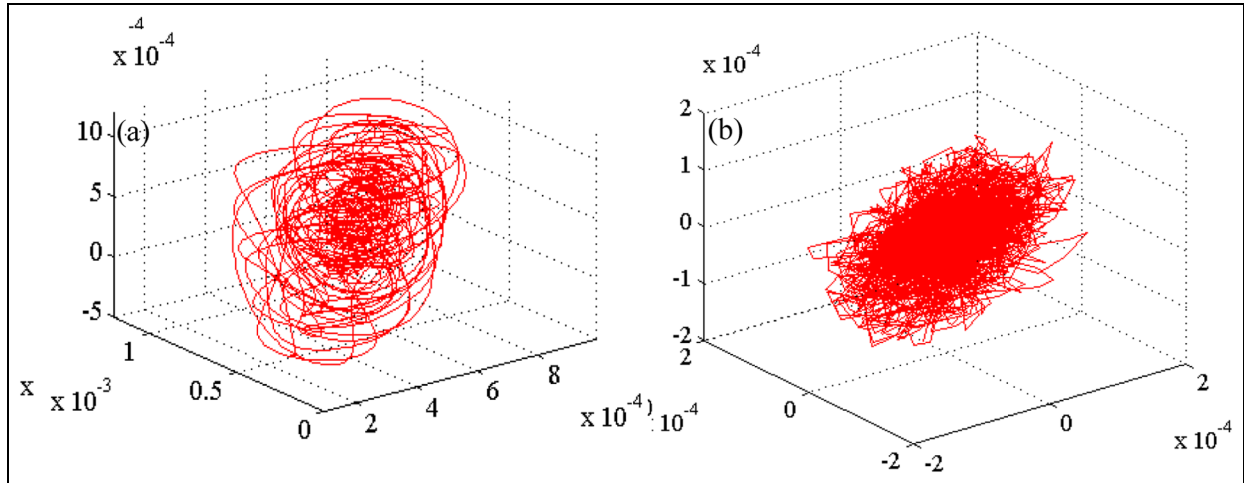


Figure 4. Reconstructed phase portraits from the structural responses under (a) Lorentz excitation and (b) wind excitations.

As the occurrence of damage is ascertained, the next order of information is to detect the location of the damage(s). The ability of the proposed MD among the phase portraits' feature in identifying the location of damage (which is inflicted at the fifth storey for single and at the third and eight stories for multiple damage

cases) are shown in Figure 6(a) and (b) for the single and multiple damage case(s), respectively. In this, the responses from all the sensor locations are assumed to be available and are normalized with respect to the maximum value of the same. The phase portraits are reconstructed for estimating the MD among the phase

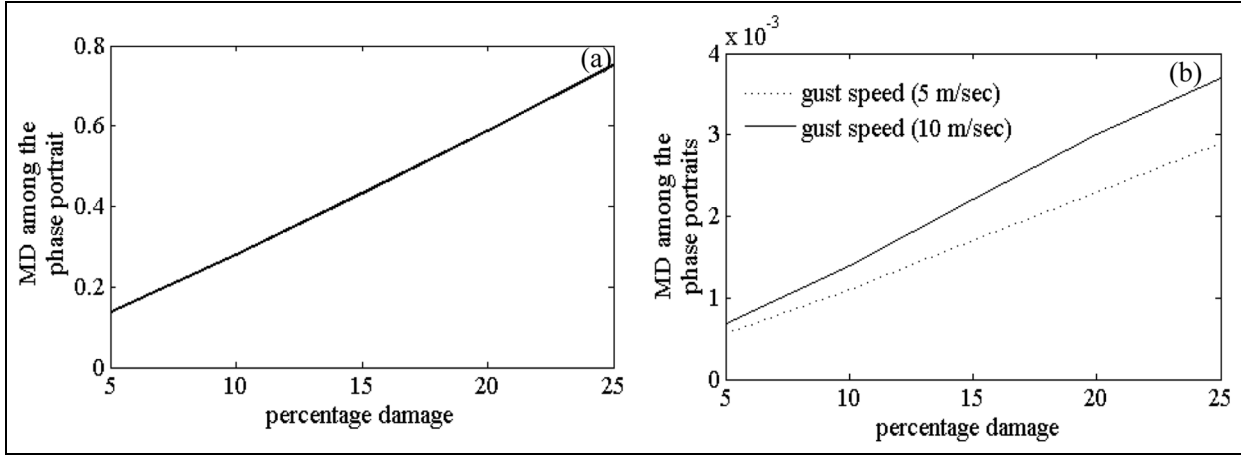


Figure 5. Variation in the MD among the phase portraits with increasing level of damage for (a) Lorentz excitations and (b) wind-induced excitations.

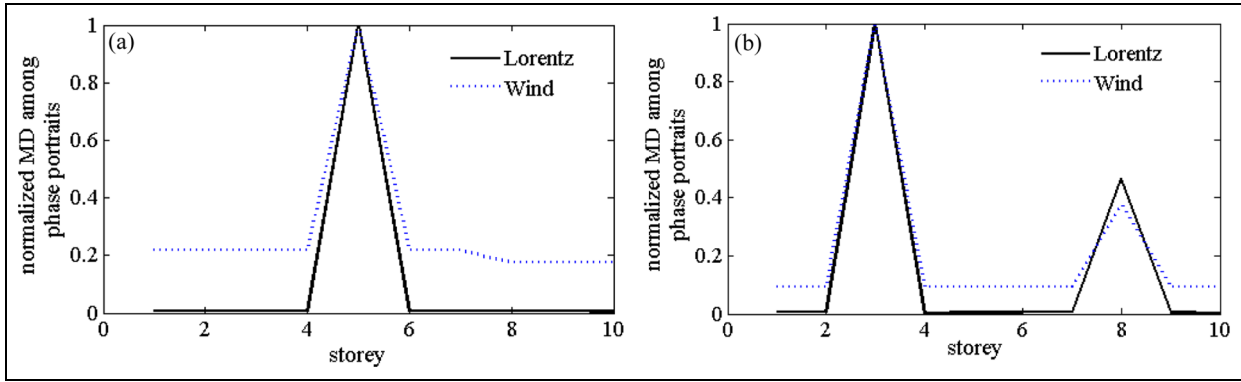


Figure 6. Efficiency of the MD among the phase portraits' feature for localizing (a) single and (b) multiple damage(s) while subjected to Lorentz and wind excitations.

portraits, pertaining to each sensor locations. The variations in the damage feature along the sensor locations are shown in Figure 6(a) and (b), indicating single and multiple damage scenarios, respectively.

It may be observed from Figure 6(a) and (b) that the MD among the phase portraits attains peak at the fifth story that happens to be the location of the (single) damage. The peak of the feature from the sensors located right at the damaged location (or around its vicinity) is in account of the fact that increasing proximity of a sensor to the damaged location will lead to increasingly higher value of the respective feature. Thus, it appears that the damage localization works satisfactorily. The localization capability under multiple damage scenarios is also demonstrated in Figure 6(b). For this, damages are induced at two stories (third and eighth) simultaneously with different severities. The presence of damages is indicated by two peaks in this plot, which correspond to the damaged locations at these stories. Furthermore, it may also be observed

that the peaks are proportional to the severity of damages and provide idea about the relative severity of the damage(s).

It is worth mentioning that the estimation of the conventional damage feature CPST involves random statistical sampling of a number of fiducial points. This renders the CPST estimate to be random with the associated mean (μ) and standard deviation (σ). However, the presently proposed MD among the phase portraits involves all the points in the phase space, and hence the feature does not involve any probabilistic variation. The mean CPST is employed to ascertain for monotonicity as well as localization of damage, as shown in Figure 7(a) and (b), respectively. The MD feature does not require the error bars associated with its estimate, unlike the CPSTs. Furthermore, the study of probabilistic robustness does not arise because of this reason, which is otherwise an important aspect to study for the conventional CPST-based damage feature based on random sampling of fiducial points on the phase portraits.

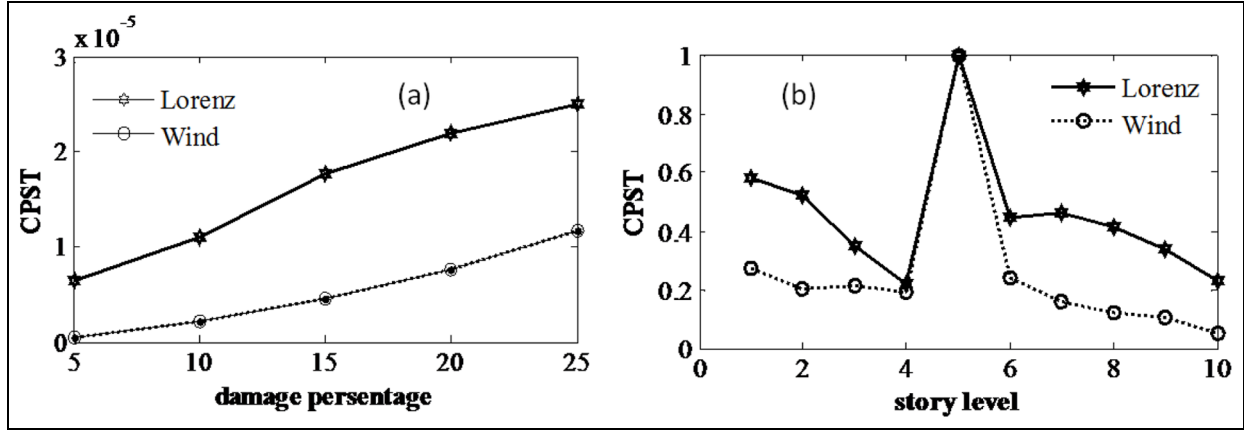


Figure 7. Damage detection using CPST: (a) monotonicity of the mean CPST with increasing damage (at fifth story) and (b) damage localization by mean CPST (25% damage).

Table 1. Computational time for CPST and MD among the phase portraits.

Input excitation	Computation time (s)	
	CPST	MD among the phase portraits
Lorenz attractor	38.465	0.011
Wind	24.321	0.003

CPST: change in phase space topology; MD: Mahalanobis distance.

Another aspect to be noted is that the estimate of the MD among the phase portraits is considerably less computation intensive than the CPST. A comparison of the CPU processing time (in a Laptop with Intel Xenon processor of 2.10 GHz speed and 16GB RAM) for both the features is provided in Table 1. As there is a continuous search for a quick damage feature in literature, the proposed one in this study might be one such alternative.

In addition to its detection and localization capability, a legitimate damage feature must be immune to intrinsic noise contamination that may arise from various sources during measurement by sensors or acquisition of response data. This is to say that the extraction of a damage feature and its capability to indicate the presence and location of damage must not be impaired by the different degrees of noise that are inherent in the measured response signals. The noise insensitivity of a feature is associated with robustness. To study this aspect, varying degrees of noises are added to the simulated response data, which are used thereafter for extraction of damage feature. The simulated noises follow Gaussian distribution and their magnitudes are determined by the degree of contamination, one would like to impose. The magnitude of noise is described by the SNR, expressed in decibel. The range of variations

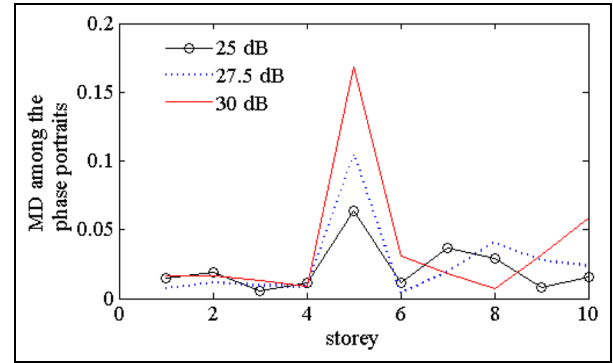


Figure 8. Damage localization capability of the MD among the phase portraits under noise contamination of responses.

considered for the SNR is from 30 to 25 dB. Such SNRs are of reasonable magnitude and the noise tolerance is tested with respect to the localization capability of damage, as shown in Figure 8, for a damage scenario with severity of 20%. Figure 8 shows that the location of damage is correctly indicated by the peak of the MD among the phase portraits' damage feature at the fifth storey under the presence of considered degree of SNR. This indicates that the damage localization capability of this feature is not impaired under the presence of some degrees of noise contamination in the response signal. The monotonicity and multiple localization are also tested and are observed to work satisfactorily with the adopted intensity of noises.

Experimental verification

The effectiveness of the MD among the phase portraits' feature for damage detection is verified with respect to an experimental dataset, obtained from the vibration

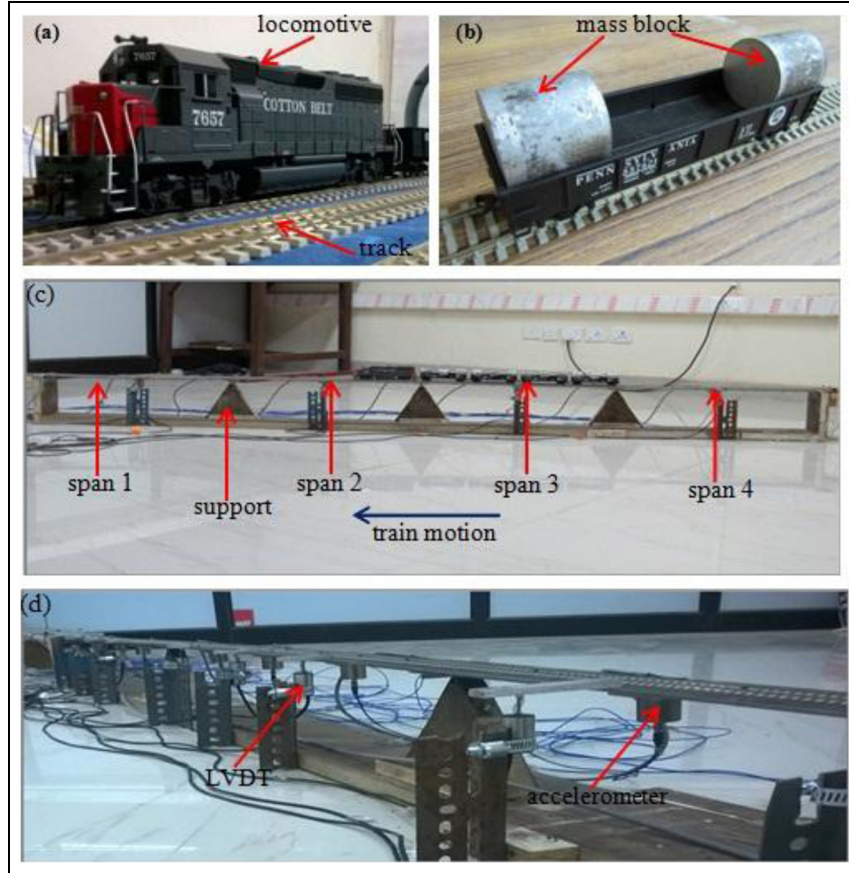


Figure 9. Scaled model for the (a) locomotive and (b) wagons (with additional weights). (c) Bridge model with the moving train and (d) bridge deck with sensors installed.

response of a model railway bridge subjected to trail of wheel loading. The experiment is conducted at the Structural Engineering Laboratory at the Indian Institute of Technology (IIT) Kanpur, UP, India. The experiment employs a model bridge. The model bridge is subjected to scaled model of a train. The bridge deck is made of steel plates of dimension $243.9 \times 7.6 \times 0.4$ cm³ supported over plywood-made wedges, simulating simply supported condition. There are totally four spans. The approach sections (150 cm long in both sides) of the bridge model are made of plywood to facilitate the starting and stopping operations of the train. Steel hinges are employed between the steel deck and plywood support to prevent uplifting of the deck from the supports.

Commercially available train model pertaining to international HO (1:87) scale is procured for the experiment. The train model consists of an engine and four freight wagons. Furthermore, additional masses of lead blocks are also added on these wagons for parametric study. The length and weight parameters for the train are provided in Table 2. The scaled train model for the locomotive and wagons is shown in Figure 9(a) and

Table 2. Weight and length parameters for the model train.

Train	Length (cm)	Mass (g)
Locomotive/engine	21.2	397
Freight wagons	16	77

(b), respectively. The rail track consists of a number of segments with 17.5 mm width and 91.5 cm length. Each segment is connected with the other segment by grooved fish plates.

The locomotive is powered through nickel silver track. A speed controller with a maximum supply of 12-V direct current is employed for controlling the train speed during experiment. The bridge model along with the moving train is shown in Figure 9(c).

The bridge deck along the spans and at the supports is instrumented by accelerometers (make: PCB Piezotronics, model: 393B04, and range $\pm 5g$), linear variable differential transformer (LVDT; make: Solarton, model: DFG, and capacity ± 5 mm), and strain gauges (make: Micro-measurements, model:

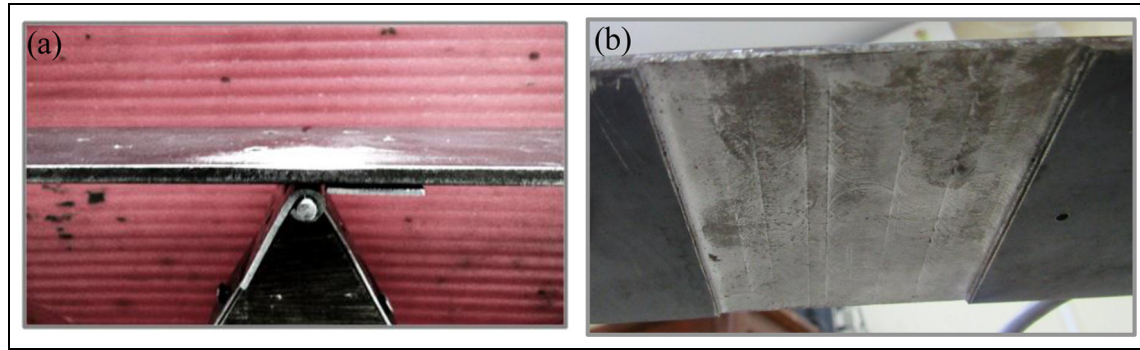


Figure 10. Simulation of two types of damage scenarios by (a) removing hinges from one side of the support and (b) cutting out the bridge section around the mid-span.

Table 3. Damage scenarios considered in the study.

Cases	Details	Damage locations
Pristine	Four-span bridge assembly	–
Support damage	Hinge 6 is opened	On support point 4 (S4)
Span damage	6 cm long and 1.5 mm deep cut out along the depth from bottom of the deck plate at 167.6 cm away from the left end (single damage)	At span 3 (between supports S3 and S4)

CEA-05). The accelerometers and LVDTs are placed at the bottom of the mid-span. Strain gauges are placed at the supports to measure the strain. An infrared light-emitting diode (LED) and photo-diode pair is placed at each end of the bridge for the purpose of recording the arrival and departure time of the train on and from the bridge, respectively. A National Instrument (NI) data acquisition system (DAQ) is employed for acquiring the sensed responses. The LabVIEW software is used to interface the monitoring in a personal computer. The sensor data are acquired through multiple channels of the DAQ. The installed sensors on the bridge are shown in Figure 9(d).

Two types of damage scenarios are considered for experimental demonstration. In the first, the damage at the supports are inflicted by removing one side of the hinges. In second scenario, the steel deck is cut to reduce the effective depth of the section at the mid-span. These are shown in Figure 10(a) and (b), respectively. These scenarios are chosen in view of the typically observed damages at the bearing as well as at the spans of the deck or in the girders supporting the deck. The responses from the damaged cases are also compared with the one from the pristine bridge. Details of these damage scenarios are tabulated in Table 3.

Parametric variations involving the train mass and the speed of the locomotive are considered while studying each damage case. These mass–speed combinations

are shown in Table 4. The four integers (digits) describe the mass combinations by referring to the number of blocks in each of the four wagons.

The MD-based damage feature relies on the displacement time history responses obtained from the LVDT installed under each span. The acquired responses are processed using low-pass Butterworth filter of fifth order with cut-off frequency of 2 Hz. The filter is run from both sides to filter out noise without causing any shift in the time history. A Tukey (tapered cosine) window with $r=0.2$ (10% of samples on each side of the data is subjected to tapering) is then applied on the measured responses. The responses are synchronized in time by shifting the time histories so that cross correlation among the time histories attains maximum. This is also to get rid of the slight speed variability of the train observed during the experiment. The MD among the phase portraits is calculated subsequently on these processed time histories.

The processed response time histories measured at the mid-span of all the spans are shown in Figure 11(a). The comparison of the response(s) of the damaged structure (for support damage case) with the pristine responses in the mid-span is also shown in Figure 11(b). The reconstructed phase portraits from the damaged-undamaged structures are shown in Figure 12. The embedding dimension employed herein is three as obtained from the singular value analysis. The

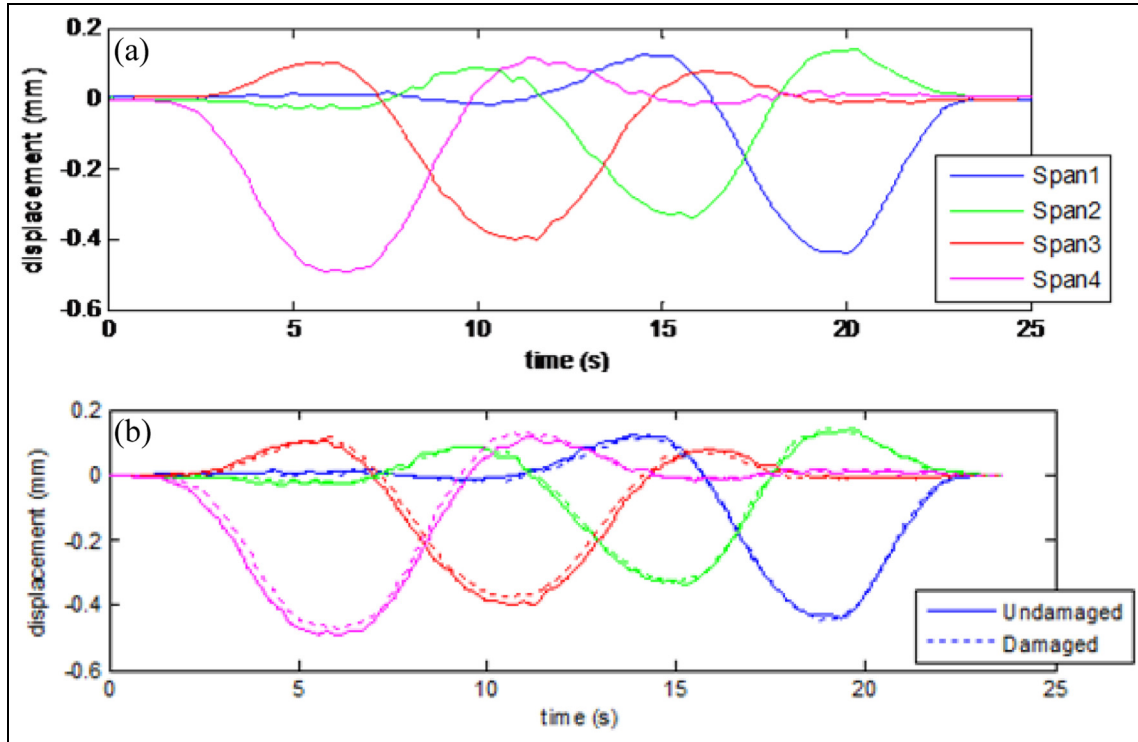


Figure 11. Deflection time histories of the bridge deck measured at the middle of (a) all the spans and (b) comparison of the damaged (support damage) and pristine response time histories measured from the sensor at span 1.

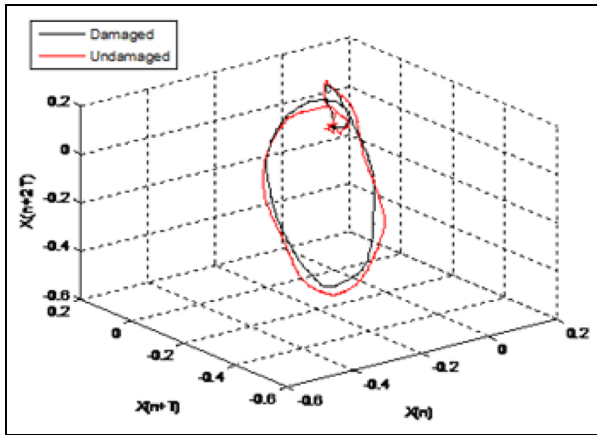


Figure 12. Phase portraits from the damaged and pristine time histories, corresponding to support damage case with M1–V1 mass–speed combinations.

respective lag coordinates are selected to be 20 as obtained from the mutual information function.

The variations in the MD among the phase portraits pertaining to all the sensor locations are shown in Figure 13(a) and (b) for the support damage case. These are indicated in Table 4 with typical speed–mass combinations. These cases involve support damage at support (hinge) number 4, which is connected between

the deck and the support toward the right side of the support. This is simulated by removing the respective leg of the hinge. The occurrence of the support damage (loosening of the hinge) is rightly pointed out by the peak observed in the variation in MD among the phase portraits along the spans shown in Figure 13(a) and (b) for different mass–speed combinations indicated therein. The measurement of the response data and subsequent estimation of the normalized MD are repeated for a number of times, to get the estimate of variability and is indicated using error bar in these plots (Figure 13(a) and 13(b)). There are slight variations observed; however, the estimates are mostly consistent. It is also important to note that as a hinge is opened in a particular side of the support, the increase in MD among the phase portraits is relatively more on the other side. This observation corroborates with the numerical simulation although not presented here for brevity.

Next, the span-wise variations in the damage feature from the bridge with span damage scenario are shown in Figure 14(a) and (b). These plots consider two different mass–speed combinations indicated in the figure. The damage(s) are simulated by cutting the bridge deck. It is noted that the localization of the damage can be attained from the variation in the MD along the sensors. For each case, the peak in the MD among the

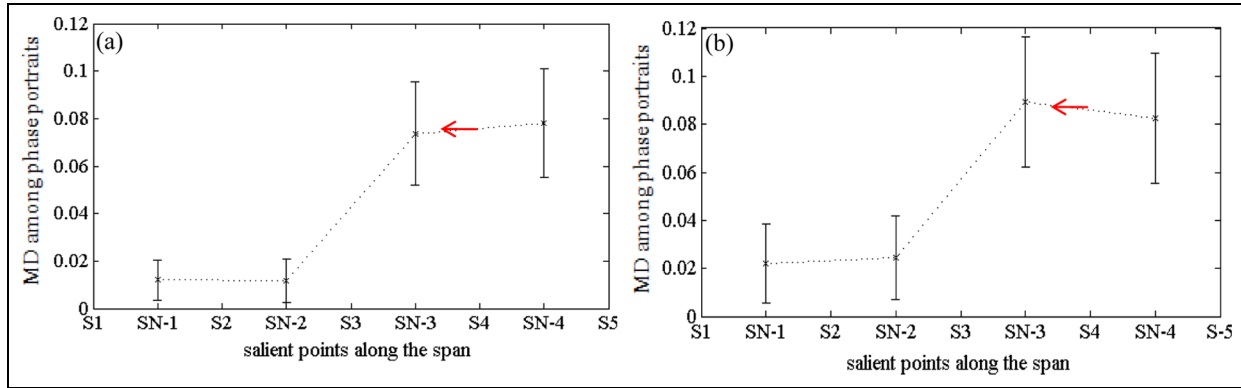


Figure 13. Variation in the normalized MD among the phase portraits estimated from the sensor data from support damage scenarios with speed-mass combinations (a) M1-V2 and (b) M2-V1. The supports are designated by S and the sensor by SN. The damage is indicated by the arrow toward the respective side.

Table 4. Details of the mass-speed combination for the wagon and locomotive.

Type of mass combinations	Mass combinations (no. of 200 g lead weight blocks on each of the four wagons)	Speed level	Speed (cm/s)
M1 (each block 200 g)	3 3 3 3	V1	15
M2 (each block 200 g)	1 3 3 1	V2	30

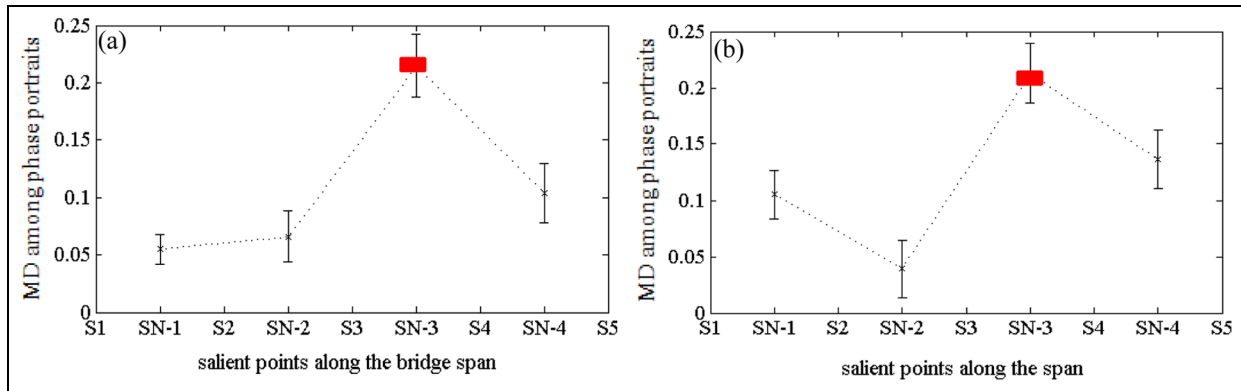


Figure 14. Variation in the normalized CPST from the sensor data pertaining to span damage scenarios with (a) M1-V2 and (b) M2-V2 mass-speed combinations. Both damages are attained by cutting along the depth. The damage location is indicated by the red block. Supports are indicated by S and sensors by SN.

phase portraits corresponds to the damage locations, thereby indicating the ability of the feature to indicate the presence and localization of damage.

The localization capability of the damage feature under operational variability of train speeds is also checked. The damage feature is computed for varying speeds of the train and its variations along the span are shown in Figure 15. Three different speed levels (varying from 15 to 45 cm/s) are considered for demonstration, and it is observed that the localization capability of the feature does not outperform under the

operational variability of the train speed, indicating to added robustness of the feature.

Conclusion

This study demonstrates that the probabilistic MD among the embedded phase portrait, reconstructed from the dynamic responses of structure, can be employed as a damage-sensitive feature for the incipient structural damage that may occur during the operational lifetime of the structure. The legitimacy of the

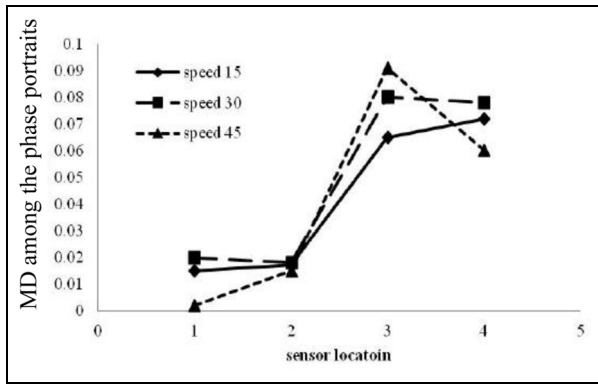


Figure 15. Localization capability of the feature under operational speed variability.

damage feature is established by demonstrating its variations with respect to various damage scenarios of increasing intensities. The damage severity and localization capability of the feature are established through numerical simulation on a shear building model. The dynamic responses employed for the feature extraction consider the low-dimensional excitations from the chaotic Lorentz system as well as natural excitations, such as wind. The noise immunity of the feature is also tested for relatively lower level of noise, which shows the necessity for improvement in this aspect. The significant efficiency in computation shows the potential of the proposed feature to qualify as a quick feature. The efficiency of the proposed feature is also demonstrated using experimental responses from a model railway bridge subjected to loading from a model train. The experimental findings show the effectiveness of the feature to indicate and localize damage both at the support of the bridge (as encountered for bearing damage) and in the middle of the span under operational variability of the train speed. An analysis is also presented in Appendix 1 that establishes the link between the damage and the resulting distortion it is causing in the phase portraits, which is quantified by the MD.

The bottlenecks, restricting the application of the phase space-based techniques, are still valid for the present feature as well. The phase space damage features are computed based on low-dimensional (narrow-band) excitations and responses. However, the present feature is easy, quick, and less computation intensive and therefore more appropriate for online monitoring comparing with other phase space-based damage features.

Acknowledgements

The authors would like to sincerely acknowledge the help from Mr Aakash Gupta for conducting the experiment. The discussions with Professor Suparno Mukhopadhyay were immensely helpful and are gratefully appreciated.

Declaration of conflicting interests

The author(s) declared no potential conflicts of interest with respect to the research, authorship, and/or publication of this article.

Funding

The author(s) received no financial support for the research, authorship, and/or publication of this article.

References

1. Doebling SW, Farrar CR, Prime MB, et al. A review of damage identification methods that examine changes in dynamic properties. *Shock Vib Digest* 1998; 30(2): 91–105.
2. Sohn H, Farrar CR, Hemez FM, et al. *A review of structural health monitoring literature: 1996–2001*. Los Alamos, NM: Los Alamos National Laboratory, 2003.
3. Salawu OS. Detection of structural damage through changes in frequency: a review. *Eng Struct* 1997; 19(9): 718–723.
4. Pandey AK, Biswas M and Samman MM. Damage detection from changes in curvature mode shapes. *J Sound Vib* 1991; 145(2): 321–332.
5. Nair KK, Kiremidjian AS and Law KH. Time series-based damage detection and localization algorithm with application to the ASCE benchmark structure. *J Sound Vib* 2006; 291(1–2): 349–368.
6. Hou Z, Noori M and St. Amand R. Wavelet-based approach for structural damage detection. *J Eng Mech* 2000; 126(7): 677–683.
7. Nichols JM. Structural health monitoring of offshore structures using ambient excitation. *Appl Ocean Res* 2003; 25: 101–114.
8. Todd MD, Nichols JM, Pecora LM, et al. Vibration based damage assessment utilizing state space geometry changes: local attractor variance ratio. *Smart Mater Struct* 2001; 10: 1000–1008.
9. Chelidze D and Liu M. Multidimensional damage identification based on phase space warping: an experimental study. *Nonlinear Dynam* 2006; 46: 61–72.
10. Nie Z, Hao H and Ma H. Using vibration phase space topology changes for structural damage detection. *Struct Health Monit* 2012; 11(5): 538–557.
11. Nie Z, Hao H and Ma H. Structural damage detection based on the reconstructed phase space for reinforced concrete slab: experimental study. *J Sound Vib* 2013; 332: 1061–1078.
12. Overbey LA, Olson CC and Todd MD. A parametric investigation of state-space-based prediction error methods with stochastic excitation for structural health monitoring. *Smart Mater Struct* 2007; 16: 1621–1638.
13. Liu G, Mao Z, Todd M, et al. Damage assessment with state-space embedding strategy and singular value decomposition under stochastic excitation. *Struct Health Monit* 2014; 13(2): 131–142.
14. Torkamani S, Butcher EA, Todd MD, et al. Hyperchaotic probe for damage identification using nonlinear

- prediction error. *Mech Syst Signal Process* 2012; 29: 457–473.
15. Mahalanobis PC. On the generalized distance in statistics. *Proc Natl Inst Sci India* 1936; 2(1): 49–55.
 16. Banerjee S, Qing XP, Beard S, et al. Prediction of progressive damage state at the hot spots using statistical estimation. *J Intell Mater Syst Struct* 2010; 21(6): 595–605.
 17. Takens F. Detecting strange attractors in turbulence. In: Rand D and Young LS (eds) *Lecture notes in mathematics*. Berlin: Springer, 1981, vol. 898, pp. 366–381.
 18. Whitney H. Differentiable manifolds. *Ann Math* 1936; 37: 645–680.
 19. Moon FC. *Chaotic vibrations: an introduction for applied scientists and engineers*. Hoboken, NJ: John Wiley & Sons, 2004.
 20. Kareem A. Numerical simulation of wind effects: a probabilistic perspective. *J Wind Eng Ind Aerod* 2008; 96: 1472–1497.
 21. Shinozuka M and Jan CM. Digital simulation of random processes and its applications. *J Sound Vib* 1972; 25(10): 111–128.
 22. Kwon D and Kareem A. NatHaz on-line wind simulator (NOWS): simulation of Gaussian multivariate wind fields. NatHaz Modeling Laboratory Report University of Notre Dame, 2006, <http://windsim.ce.nd.edu/>
 23. Davenport AG. The dependence of wind load upon meteorological parameters. In: *Proceedings of the international research seminar on wind effects on building and structure*. Toronto, ON, Canada: University of Toronto Press, 1968, pp. 19–22.
 24. Fraser AM and Swinney HL. Independent coordinates for strange attractors from mutual information. *Phys Rev A* 1986; 33(2): 1134–1140.
 25. Trickey T, Todd MD, Nichols JM, et al. Considerations for attractor property analysis in vibration based damage detection. In: *Proceedings of the SPIE5047*, San Diego, CA, July 31, 2003, pp. 340–349.
 26. Nerenberg MAH and Essex C. Correlation dimension and systematic geometric effects. *Phys Rev A* 1990; 42: 7065–7074.
 27. Stark J, Broomhead DS, Davies ME, et al. Embedding theorems for forced and stochastic systems. *Nonlinear Anal Theor Meth Appl* 1997; 30(8): 5303–5314.
 28. Orstavik S and Stark J. Reconstruction and cross-prediction in coupled map lattices using spatio-temporal embedding techniques. *Phys Letts A* 1998; 247: 145–160.
 29. <http://people.revoledu.com/kardi/tutorial/Similarity/MahalanobisDistance.html#MahalanobisDistance>
 30. Nassif HH, Gindy M and Davis J. Comparison of laser Doppler vibrometer with contact sensors for monitoring bridge deflection and vibration. *NDT&E Int* 2005; 38(3): 213–218.
 31. Feng D and Feng M. Model updating of railway bridge using in situ dynamic displacement measurement under train loads. *J Bridge Eng* 2015; 20: 04015019.
 32. George CR and Mishra SK. Structural interrogation using phase space topology of the wind induced responses. *J Vib Contr*. Epub ahead of print 5 April 2017. DOI: 10.1177/1077546317701661.
 33. Paul B, George RC and Mishra SK. Phase space interrogation of the empirical response modes for seismically excited structures. *Mech Syst Signal Process* 2016; 91: 250–265.

Appendix I

Analytical link between the distortion of the phase portraits with the damage

Detection of damage

The simplest model of a bridge is considered as a simply supported Euler beam, aligned along its longitudinal axis x . The beam has a mass density of m per unit length, a length of L , and flexural rigidity as EI , where E is the modulus of elasticity and I is the moment of inertia of the beam cross section. The flexural rigidity is denoted as $k = EI$. The Hamiltonian of the system is thus written as

$$H = \int_0^L \left[\frac{1}{2} \left\{ m \left(\frac{\partial w}{\partial t} \right)^2 + k \left(\frac{\partial^2 w}{\partial x^2} \right)^2 \right\} - q(x, t) w(x, t) \right] dx \quad (21)$$

where $w(x, t)$ is the transverse deflection and $q(x, t)$ is the lateral loading on the bridge. With simply supported ends, the deflection of the bridge can be written as

$$w(x, t) = \delta(t) \sin\left(\frac{\pi x}{L}\right) \quad (22)$$

in which $\delta(t)$ is the generalized coordinate for deflection. The transverse loading $q(x, t)$ on the bridge from the moving trail of wheels can be written as

$$q(x, t) = \sum_{i=1}^n q_i \delta(x - (vt - d_i)) \quad (23)$$

where d_i is written as

$$d_i = (i - 1)d, \quad i = 1, 2, \dots, n \quad (24)$$

in which d is the distance between two successive axles of wheels and i is the index for wheels varying from 1 to a number of axles n . q_i is the train wheel load moving with a velocity v and $\delta()$ is the Dirac delta function. In the rest of the discussion, only the summation sign is employed by dropping the number of terms n , which is implied. Substituting equations (22) and (23) into equation (21), one gets

$$H = \left(\frac{mL\dot{\delta}^2}{4} \right) + \left(\frac{k\pi^4\delta^2}{4L^3} \right) - \sum q_i \delta \sin\left(\frac{\pi(vt - d_i)}{L}\right) \quad (25)$$

The gradient of the Hamiltonian with respect to the generalized coordinates can be expressed as

$$\frac{\partial H}{\partial \delta} = \frac{k\pi^4\delta}{2L^3} - \sum q_i \sin\left(\frac{\pi(vt - d_i)}{L}\right); \frac{\partial H}{\partial \dot{\delta}} = \frac{mL}{2} \dot{\delta} \quad (26)$$

Using the relationship

$$\frac{dx_1}{dt} = -\frac{\partial H}{\partial \delta}; \frac{dx_2}{dt} = \frac{\partial H}{\partial \dot{\delta}} \quad (27)$$

The ordinates of the phase space can be expressed as

$$\begin{aligned} \frac{dx_1}{dt} &= -\frac{k\pi^4\delta}{2L^3} + \sum q_i \sin\left(\frac{\pi(vt - d_i)}{L}\right) \\ \frac{dx_2}{dt} &= \frac{mL}{2} \dot{\delta} \end{aligned} \quad (28)$$

Using the assumed spatial displacement profile, the generalized stiffness, mass, and loading can be expressed as

$$\begin{aligned} \bar{m} &= \int_0^L m \sin^2\left(\frac{\pi x}{L}\right) dx = \frac{mL}{2}; \bar{k} = k \left(\frac{\pi^4}{L^4} \right) \\ \int_0^L \sin^2\left(\frac{\pi x}{L}\right) dx &= \left(\frac{k\pi^4}{2L^3} \right) \\ \bar{q} &= \int_0^L q(x, t) \sin\left(\frac{\pi x}{L}\right) dx = \sum q_i \sin\left(\frac{\pi(vt - d_i)}{L}\right) \end{aligned} \quad (29)$$

The natural frequency and the frequency of loading thus become

$$\omega_n = \left(\frac{\pi^2}{L^2} \right) \left(\sqrt{\frac{k}{m}} \right); \omega = \frac{\pi v}{L} \quad (30)$$

The generalized responses are then obtained as

$$\begin{aligned} \delta(t) &= \sum \frac{2q_i L^3}{(k\pi^4 - mL^2\pi^2 v^2)} \sin\left(\frac{\pi(vt - d_i)}{L}\right); \\ \dot{\delta}(t) &= \sum \frac{2q_i \pi v L^2}{(k\pi^4 - mL^2\pi^2 v^2)} \cos\left(\frac{\pi(vt - d_i)}{L}\right) \end{aligned} \quad (31)$$

Substituting equation (27) into equation (26), the phase space coordinates become

$$\begin{aligned} x_1 &= \sum \left\{ \frac{mvq_i L^3}{\pi(k\pi^2 - mL^2 v^2)} \right\} \cos\left(\frac{\pi(vt - d_i)}{L}\right) \\ x_2 &= - \sum \frac{mvq_i L^3}{\pi(k\pi^2 - mL^2 v^2)} \frac{L}{\pi v} \sin\left(\frac{\pi(vt - d_i)}{L}\right) \end{aligned} \quad (32)$$

Localizing the phase portrait for a single-axis loading and eliminating the time dependency, the phase portrait forms an ellipse in two-dimensional (x_1, x_2) phase space with the shape of the phase portrait as an ellipse with major and minor axes as

$$a = \left\{ \frac{mvq_i L^3}{\pi(k\pi^2 - mL^2 v^2)} \right\}; b = \left\{ \frac{mvq_i L^3}{\pi(k\pi^2 - mL^2 v^2)} \right\} \frac{L}{\pi v} \quad (33)$$

The ratio of minor to major axis is then expressed as

$$\left(\frac{b}{a} \right) = \frac{L}{\pi v} \quad (34)$$

It can be observed that for a particular speed of train, the frequency of the loading remains identical and so is this ratio. The mean anomaly time-averaged distance of the points on this elliptical phase portrait from the focus can be expressed as

$$\bar{r} = \frac{3a}{2} - \frac{b^2}{2a} \quad (35)$$

This change in this distance due to damage may be evaluated by taking differential of this distance as

$$\Delta \bar{r} = \left(\frac{3}{2} \right) \Delta a + \left(\frac{1}{2} \right) \left(\frac{b}{a} \right)^2 \Delta a - \left(\frac{b}{a} \right) \Delta b \quad (36)$$

These differentials are evaluated as

$$\Delta a = - \frac{mvq_i \pi L^3}{(k\pi^2 - mL^2 v^2)^2} \Delta k; \Delta b = - \frac{mvq_i \pi L^3}{(k\pi^2 - mL^2 v^2)^2} \frac{L}{\pi v} \Delta k \quad (37)$$

Substituting equation (32) into equation (31), we obtain

$$\Delta \bar{r} = \frac{\Delta k}{2} \left\{ \left(\frac{L}{\pi v} \right)^2 - 3 \right\} \frac{mvq_i \pi L^3}{(k\pi^2 - mL^2 v^2)^2} \quad (38)$$

This $(\Delta \bar{r})$ can be taken as an average estimate of the distortion of the phase portrait due to induced change in stiffness (Δk) . It is observed that the change in the distortion is proportional to the change in stiffness; however, with increasing value of the stiffness, the change diminishes to some extent as the stiffness term contributes predominantly to the denominator in equation (33). Furthermore, with increasing magnitude of

the wheel loading, the distortion increases and so is the effect of the exciting frequency. This also implies that a higher speed of train would help in detection by enhancing the sensitivity of the damage index.

Localization of the damage

For localization, let us assume that the damage in the form of stiffness change (Δk) is introduced at a position ($x = x_0$) on the undamaged stiffness (k) along the beam. The stiffness is then written as

$$k(x) = k + \Delta k \delta(x - x_0) \quad (39)$$

Assuming the spatial variation in the displacement field as in equation (22), the estimate of the Hamiltonian is then written as

$$H = \left(\frac{mL\dot{\delta}^2}{4} \right) + \left(\frac{k\pi^4\delta^2}{4L^3} \right) - \sum q_i \delta \sin\left(\frac{\pi(vt - d_i)}{L}\right) + \left(\frac{\Delta k \delta^2 \pi^4}{2L^4} \right) \sin^2\left(\frac{\pi x_0}{L}\right) \quad (40)$$

Proceeding similarly as earlier, the major and minor axes of the elliptical phase portrait for a single-axle wheel loading become

$$a = \frac{q_i m L^3 v}{\pi(k\pi^2 - mL^2 v^2)} + \frac{2\Delta k q_i \pi^3}{v(k\pi^4 - mL^2 \pi^2 v^2)} \sin^2\left(\frac{\pi x_0}{L}\right) \\ b = \frac{m q_i v L^3}{\pi(k\pi^2 - mL^2 v^2)} \frac{L}{\pi v} \quad (41)$$

It may be observed that while the major axis is influenced by the induced damage, the minor axis is not. The ratio of the major to minor axis may still be assumed to be the same as in equation (34), and then the changes in the major axis (Δa) due to damage ($\Delta k \delta(x - x_0)$) may be written as

$$\Delta a = \left(\frac{2q_i \pi^3 \Delta k}{v\pi^2(k\pi^2 - mL^2 v^2)} \right) \sin^2\left(\frac{\pi x_0}{L}\right) \quad (42)$$

It is also noted that there is no change in the minor axis due to induced damage, that is, ($\Delta b = 0$). The change in the average distance ($\Delta \bar{r}$) from the ellipse can then be written as

$$\Delta \bar{r} = \frac{\pi q_i \Delta k}{v(k\pi^2 - mL^2 v^2)} \left\{ 3 + \left(\frac{L}{\pi v} \right)^2 \right\} \sin^2\left(\frac{\pi x_0}{L}\right) \quad (43)$$

This indicates that if there is a damage localized at ($x = x_0$), there will be a respective jump in the estimate ($\Delta \bar{r}$) at that location which helps in localizing the damage at the location.